1-1-2014

Lithium migration in Li4Ti5O12 studied using in-situ neutron powder diffraction

Wei Kong Pang
University of Wollongong, wkpang@uow.edu.au

Vanessa Peterson
ANSTO, vep@ansto.gov.au

Neeraj Sharma
Univerity of New South Wales

Je-Jang Shiu
Tatung University Taipei

She-Huang Wu
Tatung University Taipei

Lithium migration in Li4Ti5O12 studied using in-situ neutron powder diffraction

Abstract

We used in situ neutron powder diffraction (NPD) to study the migration of Li in Li4Ti5O12 anodes with different particle sizes during battery cycling. The motivation of this work was to uncover the mechanism of the increased capacity of the battery made with a smaller-particle-sized anode. In real time, we monitored the anode lattice parameter, Li distribution, and oxidation state of the Ti atom, and these suggested an increase in the rate of Li incorporation into the anode rather than a change in the migration pathway as a result of the particle size reduction. The lattice of these anodes during continuous lithiation undergoes expansion followed by a gradual contraction and then expansion again. The measured lattice parameter changes were reconciled with Li occupation at specific sites within the Li4Ti5O12 crystal structure, where Li migrates from the 8a to 16c sites. Despite these similar Li-diffusion pathways, in larger-particle-sized Li4Ti5O12 the population of Li at the 16c site is accompanied by Li depopulation from the 8a site, which is in contrast to the smaller-particle-sized anode where our results suggest that Li at the 8a site is replenished faster than the rate of transfer of Li to the 16c site. Fourier-difference nuclear density maps of both anodes suggest that 32e sites are involved in the diffusion pathway of Li. NPD is again shown to be an excellent tool for the study of electrode materials for Li-ion batteries, particularly when it is used to probe real-time crystallographic changes of the materials in an operating battery during charge-discharge cycling.

Keywords

in-situ neutron diffraction, lithium ion battery, lithium titanium oxide, particle size, lithiation and delithiation mechanism

Disciplines

Engineering | Science and Technology Studies

Publication Details

Pang, W., Peterson, V., Sharma, N., Shiu, J. & Wu, S. (2014). Lithium migration in Li4Ti5O12 studied using in-situ neutron powder diffraction. Chemistry of Materials, 26 (7), 2318-2326.

Lithium migration in $Li_4Ti_5O_{12}$ studied using in-situ neutron powder diffraction

Wei Kong Pang[1,2], Vanessa K. Peterson[1,*], Neeraj Sharma[3], Je-Jang Shiu[4], She-huang Wu[4,*]

[1] The Bragg Institute, Australian Nuclear Science and Technology Organization, Locked Bag 2001, Kirrawee DC, NSW 2232, Australia.

[2] School of Mechanical, Materials, and Mechatronic Engineering, Institute for Superconducting & Electronic Materials, Faculty of Engineering, University of Wollongong, NSW 2522, Australia.

[3] School of Chemistry, University of New South Wales, Sydney NSW 2052, Australia.

[4] Department of Materials Engineering, Tatung University, No.40, Sec. 3, Zhongshan N. Rd., Taipei City 104, Taiwan (R.O.C).

*Corresponding authors.

KEYWORDS: in-situ neutron diffraction, lithium ion battery, lithium titanium oxide, particle size, lithiation and delithiation mechanism.

ABSTRACT: We use in-situ neutron powder diffraction (NPD) to study the migration of Li in $Li_4Ti_5O_{12}$ anodes with different particle sizes during battery cycling. The motivation of this work was to uncover the mechanism for increased capacity of the battery made with a smaller particle-sized anode. We monitor in real time the anode lattice parameter, Li distribution, and the oxidation state of the Ti atom, with these suggesting an increase in the rate of Li incorporation into the anode rather than a change in migration pathway as a result of the particle size reduction. The lattice of these anodes during continuous lithiation undergoes expansion, followed by a gradual contraction, and lastly expansion again. The measured lattice parameter changes are reconciled with Li occupation at specific sites within the $Li_4Ti_5O_{12}$ crystal structure, where Li migrates from the 8*a* to 16*c* sites. Despite these similar Li diffusion pathways, in the larger particle-sized $Li_4Ti_5O_{12}$ the population of Li at the 16*c* site is accompanied by Li depopulation from the 8*a* site, in contrast to the smaller particle-sized anode where our results suggest that the Li at the 8*a* site is replenished faster that the rate of transfer of Li to the 16*c* site. Fourier-difference nuclear density maps of both anodes suggest that 32*e* sites are involved in the diffusion pathway of Li. NPD is again shown to be an excellent tool for the study of electrode materials for Li-ion batteries, particularly when used to probe the real-time crystallographic changes of the materials in an operating battery during charge-discharge cycling.

■ INTRODUCTION

Since Sony Corporation introduced the first commercial Li-ion battery (LIB) in 1991, featuring $LiCoO_2$ and graphite as the cathode and anode, respectively, LIBs are now extensively used for energy storage due to their relatively high energy density, long cycle life, and low cost.[1] However, increasing demands placed on LIBs for better electrochemical performance and safer operation mandate the further development of battery materials.

Spinel $Li_4Ti_5O_{12}$ is a well-known zero-strain insertion compound that is an alternative anode to the widely-used carbonaceous materials. This is because $Li_4Ti_5O_{12}$ shows exceptionally high rate performance, excellent cycling stability, and good Li-insertion electrochemistry with a formal potential of ~1.55 V vs. Li^+/Li as an anode in LIBs.[2-6] As a result of the high redox potential of $Li_4Ti_5O_{12}$, the formation of a solid electrolyte interface layer[7-10] and Li-metal deposition or electroplating[11] on the surface of the anode, all detrimental to LIB use, can be prevented. It is generally accepted that the Li (de)intercalation reaction in $Li_4Ti_5O_{12}$ proceeds through a reversible two-phase reaction (Eq. 1), resulting in flat plateaus of the charge and discharge curves.

$$(\mathrm{Li})^{8a}(\mathrm{Li}_{1/3}\mathrm{Ti}_{5/3})^{16d}\mathrm{O}_4{}^{32e} + x\mathrm{e}^- + x\mathrm{Li}^+ \xleftrightarrow{\sim 1.55\ \mathrm{V}} (1\text{-}x)(\mathrm{Li})^{8a}(\mathrm{Li}_{1/3}\mathrm{Ti}_{5/3})^{16d}\mathrm{O}_4{}^{32e} + x(\mathrm{Li}_2)^{16c}(\mathrm{Li}_{1/3}\mathrm{Ti}_{5/3})^{16d}\mathrm{O}_4{}^{32e} \quad \text{(Eq. 1)}$$

where the superscripts are the crystallographic sites. The $(\mathrm{Li})^{8a}(\mathrm{Li}_{1/3}\mathrm{Ti}_{5/3})^{16d}\mathrm{O}_4{}^{32e}$ and $(\mathrm{Li}_2)^{16c}(\mathrm{Li}_{1/3}\mathrm{Ti}_{5/3})^{16d}\mathrm{O}_4{}^{32e}$ crystallize in the $Fd\bar{3}m$ space group with similar lattice parameters and are referred to as $Li_4Ti_5O_{12}$ and $Li_7Ti_5O_{12}$, respectively. The difference in the lattice parameter of $Li_4Ti_5O_{12}$ and $Li_7Ti_5O_{12}$ is less than 0.1%, with the latter lattice being slightly smaller.[3, 4].

In both phases 1/6 of 16*d* sites are occupied by "electrochemically inert" Li^+ with the remainder being Ti^{4+}. The "electrochemically active" Li^+ occupies tetrahedral (8*a*) sites in $Li_4Ti_5O_{12}$. During charge (Li insertion) and minimizing strain, the "electrochemically active" Li^+ is re-located to the octahedral (16*c*) sites, together with the newly inserted Li^+, forming $Li_7Ti_5O_{12}$. In contrast to this more popular theory,[2-6] Wagemaker *et al*. report that the two-phase system is only found at temperatures below 100 K and that single-phase $Li_4Ti_5O_{12}$ is found at room temperature where a gradual change in the $Li_4Ti_5O_{12}$ lattice parameter occurs during charge in a process where mixed 8*a*/16*c* occupation by Li exists.[12] The high rate capability of $Li_{4+z}Ti_5O_{12}$ ($z = 0 \sim 3$) is attributed to solid-solution-induced disorder involving the mixed 8*a*/16*c* occupation.[12] Wagemaker *et al.* report the Li (de)intercalation of $Li_4Ti_5O_{12}$ to occur via the following solid-solution reaction (Eq. 2):

$$(\mathrm{Li})^{8a}(\mathrm{Li}_{1/3}\mathrm{Ti}_{5/3})^{16d}\mathrm{O}_4{}^{32e} + x\mathrm{e}^- + x\mathrm{Li}^+ \xleftrightarrow{\sim 1.55\ \mathrm{V}} (\mathrm{Li}_{1-y})^{8a}(\mathrm{Li}_{x+y})^{16c}(\mathrm{Li}_{1/3}\mathrm{Ti}_{5/3})^{16d}\mathrm{O}_4{}^{32e} \quad \text{(Eq. 2)}$$

where $x, y \leq 1$.

The phase transition between $Li_4Ti_5O_{12}$ and $Li_{4+z}Ti_5O_{12}$ (or $Li_7Ti_5O_{12}$ in the two-phase mechanism) involves a relatively small change in lattice parameters and similar crystal structures. Notably, the underlying mechanism of the phase transition remains controversial and, importantly, may control the performance of the $Li_4Ti_5O_{12}$ anodes. For example, it is known that electrodes prepared by different methods with correspondingly different particle sizes can have different electrochemical performance, led by a distribution of redox potentials in the near-surface area, more contact area with electrolyte, and shorter Li diffusion distance.[13-18] Thus, characterizing the Li^+ insertion/extraction mechanisms of samples with different particle-sizes will yield insight into how battery performance may be improved by modifying the $Li_4Ti_5O_{12}/Li_7Ti_5O_{12}$ anode.

Increasingly, neutron powder diffraction (NPD) has been used to study LIBs. Cai *et al.*[19] used in-situ NPD to study the inhomogeneous degradation of electrodes in large-format LIBs, and Sharma *et al.*[20-25] used in-situ NPD to study the non-equilibrium phase transitions of electrodes in LIBs. In particular, the relatively large penetration depth and non-destructive interaction of neutrons with matter allows NPD to probe in real-time the bulk crystallography of electrodes in functioning batteries. The sensitivity of NPD to light elements such as Li and O in the presence of heavier ones, can also enable the direct measurement of the Li content and its location within electrodes at the same time as the determination of redox-active couples by tracking the transition-metal valence via the oxygen to transition-metal distance. With these advantages, NPD can be useful in studying near zero-strain materials such as $Li_4Ti_5O_{12}$ during battery function. Colin *et al.*[26] tracked the Li occupation during its migration from the 8*a* to the 16*c* site in $Li_7Ti_5O_{12}$ by examining the evolution of the $Li_7Ti_5O_{12}$ 773 and 666 reflection intensity with battery charge using NPD. More recently, our work[21] correlated the Ti oxidation state to the intensity of the $Li_4Ti_5O_{12}$ 222 reflection by studying the change in the O positional parameter during charge/discharge cycling in a $LiNi_{0.5}Mn_{1.5}O_4||Li_4Ti_5O_{12}$ full cell.

In this work, we determine using in-situ NPD the phase evolution of two $Li_4Ti_5O_{12}$ anode materials prepared by different methods, where we determine the materials to have different particle sizes and electrochemical performance, but the same phase composition and crystallography. $Li_4Ti_5O_{12}$ is the limiting electrode in the neutron-friendly battery, which was assembled using deuterated electrolyte and the relatively well-studied olivine $LiFePO_4$ cathode, the latter having many merits as an advanced cathode material having been commercially used for large-format LIBs since its introduction by Padhi *et al.* in 1997.[27, 28] We examined the lithiation/delithiation mechanism of the $Li_4Ti_5O_{12}$ alongside the typical two-phase transition of $LiFePO_4$ by galvanostatically charging and discharging the battery within the 1.0 – 3.0 V window (vs. $Li_4Ti_5O_{12}$). We also investigated the formation of $Li_{4+z}Ti_5O_{12}$ by applying a 5-hour potentiostatic regime at 3.0 V. The diffusion path of Li within the anode during charge and discharge is proposed based on analysis of the in-situ NPD. The dissimilarities between the functionality of two $Li_4Ti_5O_{12}$ anodes are uncovered and discussed.

■ EXPERIMENTAL

$LiFePO_4$ cathode powders were provided by Tatung Fine Chemicals Co., Taiwan. $Li_4Ti_5O_{12}$ anode powders were prepared with different particle sizes. The larger particle-sized $Li_4Ti_5O_{12}$ (LTO-1) was prepared using a sol-gel method using lithium nitrate (100%, Wako) and titanium butoxide (98.0%, Acros). The stoichiometrically-mixed powders (Li:Ti = 4:5) were added to a solution of citric acid (CA) (99.5%, Acros) and ethylene glycol (EG) (99.5%, Acros) (CA : EG = 1 : 4) at 85 °C for 5 hours to become sols. The sols were heated at 100 and 180 °C to remove water and excess EG, respectively, and to form gels. The gels were then calcined at 350 °C for 4 hours, followed by heat-treatment at 850 °C for 10 hours. $Li_4Ti_5O_{12}$ powders with a smaller particle-size (LTO-2) were also prepared via a sol-gel method, but using lithium acetate (98%, Acros) instead of lithium nitrate. The stoichiometrically mixed powders were dissolved in an adequate amount of ethanol (99.5%, Shimakyu) and the solution aged for 3 hours to form a white-colored gel. The resulting gel was heated at 80 °C to yield an organic precursor with a fine white product powder obtained by heat-treating in air at 800 °C for 4 hours.

High-resolution NPD data were collected using ECHIDNA, the high-resolution neutron powder diffractometer at the Open Pool Australian Light-water (OPAL) research reactor at the Australian Nuclear Science and Technology Organisation (ANSTO).[29] The neutron beam wavelength was 1.6214(4) Å, determined using the $La^{11}B_6$ NIST standard reference material 660b. The NPD data were obtained in the 2θ angular range 4 to 164° with a step size of 0.125°. Rietica ver. 1.77[30] was employed to perform Rietveld analysis of the high-resolution NPD data. The refineable parameters include the background coefficients, zero-shift, peak shape parameters, lattice parameters, O positional parameter, and isotropic atomic displacement parameters.

The morphology of the as-prepared samples was investigated using field-emission scanning electron microscopy with a SU8000 (Hitachi, Japan). All observations were carried out without a conductive coating a 10 kV acceleration voltage. The particle size distribution of the as-prepared samples were

examined using a LS 13 320 (Beckman Coulter, Canada) particle size analyzer.

Specially designed pouch-type batteries were used in the collection of in-situ NPD data from the LTO-1 and LTO-2 anodes. The $LiFePO_4$ cathode was prepared by casting a slurry of the active materials (80 wt.%), acetylene black (10 wt.%), and polyvinylidene difluoride (PVDF) binder (10 wt.%) onto Al foil. The loading ratio between the anode and cathode was designed to be ~ 4:6 by weight. The electrodes were cut into 1 × 4 cm strips. Immobilon–P PVDF membrane (Millipore) was used as a separator due to its lower H content relative to the conventionally-used Celgard membrane, where the strong incoherent neutron scattering of H is detrimental to the NPD signal. The $LiFePO_4||Li_4Ti_5O_{12}$ batteries were prepared by stacking 30 anode/separator/cathode assemblies with a parallel connection. The stack was placed in an Ar-filled glove box for 24 hours and then wrapped in a polypropylene-coated Al foil to form a pouch. The dimension of the prepared cell was 1.5 cm wide (including the sealing junction of the Al pouch), 10 cm long (including electrode handles), and 1 cm thick. Prior to the in-situ NPD experiment, deuterated electrolyte solution (1 M lithium hexafluorophosphate (99.99%, Sigma-Aldrich) in a 1:1 volume ratio of deuterated dimethyl carbonate (99.5%, Novachem) to deuterated ethylene carbonate (98%, Novachem) was injected into the pouch which was heat-sealed under Ar. After 1-day of wetting, the batteries were used in the in-situ NPD experiment. The batteries containing LTO-1 and LTO-2 anodes are termed "battery-1" and "battery-2", respectively. During the in-situ NPD experiment both batteries were cycled galvanostatically using a potentiostat/galvanostat (Autolab PG302N) at currents of 11 mA (theoretically equivalent to 0.1 C) for 2 cycles between 1.0 and 3.0 V (vs. $Li_4Ti_5O_{12}$). In the second cycle, a constant voltage step at 3.0 V for 5 hours was applied.

In-situ NPD data of the $LiFePO_4||Li_4Ti_5O_{12}$ batteries were collected using WOMBAT,[31] the high-intensity neutron powder diffractometer at the OPAL research reactor at ANSTO. WOMBAT features an area detector that continuously covers 120º in 2θ and has a relatively intense neutron beam, allowing the rapid collection of data. A neutron beam with a wavelength of 2.9592(2) Å was used, determined using the $La^{11}B_6$ NIST Standard Reference Material 660b. The diffractograms were obtained with an exposure time of 5 minutes per pattern in the angular range 16.1 - 136.9° in 2θ during charge-discharge cycling of the batteries. Sequential Rietveld refinements were carried out using the NPD data using Fullprof with visualization in WinplotR.[32, 33] The refinements were performed using data in the range 60 - 120° in 2θ. Single-peak fitting of the $LiFePO_4$ 211 and 311 reflections, the $FePO_4$ 222 reflection, and the $Li_{4+z}Ti_5O_{12}$ 004 reflection was performed using the Large Array Manipulation Program (LAMP).[34]

■ RESULTS AND DISCUSSION

Using high resolution NPD data, the crystallographic details of the $LiFePO_4$, LTO-1, and LTO-2 was established. $LiFePO_4$ was found to adopt the orthorhombic *Pnma*[35] space group symmetry and the refined-fit profile is shown in **Figure S1** and crystallographic details obtained from Rietveld analysis in **Table S1**. Both LTO-1 and LTO-2 adopt $Fd\bar{3}m$ space group symmetry. In addition to the main $Fd\bar{3}m$ phase, a minor amount of monoclinic Li_2TiO_3 was also detected, 4.8(6) and 1.9(3) wt.% in LTO-1 and LTO-2, respectively. The Rietveld-refinement profiles for LTO-1 and LTO-2 are shown in **Figure 1a** and **b,** respectively. The crystallographic details are summarized in **Table S1** and indicate similar crystallographic features between LTO-1 and LTO-2.

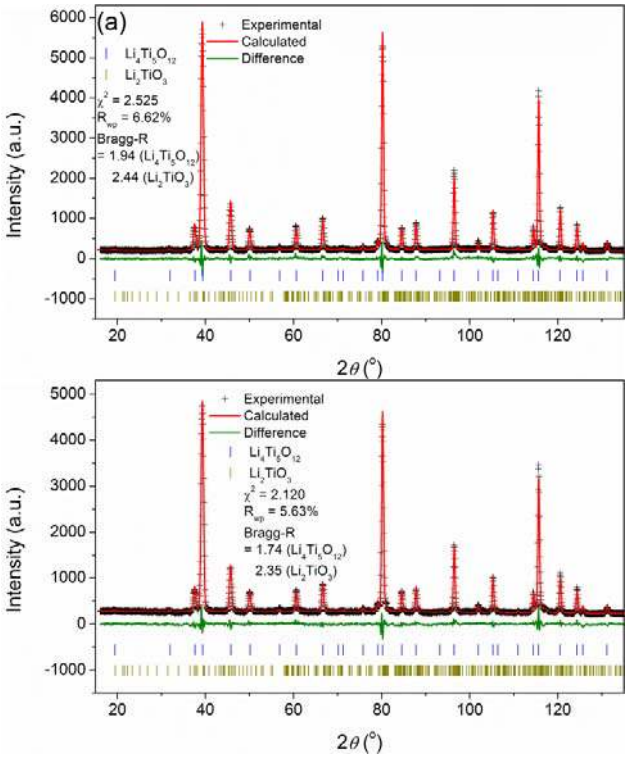

Figure 1. Rietveld profile fits for (a) LTO-1 and (b) LTO-2 using high-resolution NPD data. Measured data are shown as crosses and the calculation is the solid line through these. The difference between the measured and calculated patterns is shown along the bottom of the plots. The figures of merit include the Bragg statistical reliability factor (Bragg-R), the profile factor (R_p), the weighted profile factor (R_{wp}), and the goodness-of-fit (χ^2) term. Vertical bars represent the reflection positions for each of the phases. Profile fit for $LiFePO_4$ is also shown in Figure S1.

The particle size and morphology of the as-prepared electrode materials are shown in the SEM micrographs in **Figure 2**. The $LiFePO_4$ particles are bar-like and ~1 micron wide and ~3.5 micron long. Both LTO-1 and LTO-2 are cube-like and differ significantly in their average particle-sizes, with SEM showing LTO-1 to have an average primary particle-size of ~ 500 nm and LTO-2 of ~200 nm. Particle size distributions are shown in the inset of Figure 2, with mean particle sizes that, like the SEM analysis, show LTO-1 particles to be approximately twice as large as LTO-2 particles. The larger particle size determined in the particle size distribution analysis relative to that obtained using SEM likely arises because of the measurement of agglomerates (the secondary particle size).

The collected NPD patterns of battery-1 and battery-2 during cycling are shown in **Figure S3**. Single-peak fitting routines applied to the $LiFePO_4$ 211 and 311 reflections and the $FePO_4$ 221 reflection in the in-situ NPD data are plotted in **Figure S4**.

The results show that for both batteries the $LiFePO_4$ reflection positions remain nearly unchanged during the battery charge and discharge, but that the $LiFePO_4$ reflection intensities decrease with increasing $FePO_4$ 221 reflection intensity during battery charge. On discharge the $LiFePO_4$ reflection intensities increase with decreasing $FePO_4$ reflection intensities, suggesting that a two-phase reaction occurs during lithiation and delithiation of the $LiFePO_4$ cathode, in agreement with previous work.[27, 28]

We model the lattice evolution of the $Li_{4+z}Ti_5O_{12}$ anode as a single-phase (solid-solution reaction) after Wagemaker *et al,*[12] the details of which are presented in **Table S2**. The Rietveld-refined fit profiles of battery-1 and battery-2 are shown in **Figure S5a** and **b,** and the ranges of figures-of-merit, including χ^2, R_{wp}, and Bragg-R factors, are summarized in **Table S3**.

We first consider the phase fraction of the active materials inside the batteries. Before cycling Rietveld analysis shows that the two batteries have the similar anode to cathode weight ratio of (45:55), in agreement with their construction. During charging the phase fraction of $LiFePO_4$ decreases monotonically with increasing fraction of $FePO_4$ as a result of the two-phase reaction found from the single peak fitting. The phase fraction of the $Li_{4+z}Ti_5O_{12}$ remains relatively stable (**Figure 3**), as expected from the solid-solution model. In comparison, we note that a relatively higher phase fraction of $FePO_4$ is found in battery-2 than in battery-1 and that this is correlated to the higher capacity of battery-2. At the same anode to cathode weight ratio and same applied current, we find that LTO-2 exhibits a better rate capability than LTO-1, as expected from the smaller particle-sized LTO-2.

Besides the variation of phase composition, the details of the $Li_{4+z}Ti_5O_{12}$ lattice during charge and discharge are also extracted. Interestingly, the NPD data reveals that the $Li_{4+z}Ti_5O_{12}$ lattice is perturbed from a simple contraction during charge (Li insertion) and expansion during discharge (Li extraction), see **Figure 4**. Single peak fitting results support this unexpected observation. Notably, this work finds that during continuous lithiation both anodes undergo the following processes: Lattice expansion, followed by a gradual contraction, followed finally by further expansion.

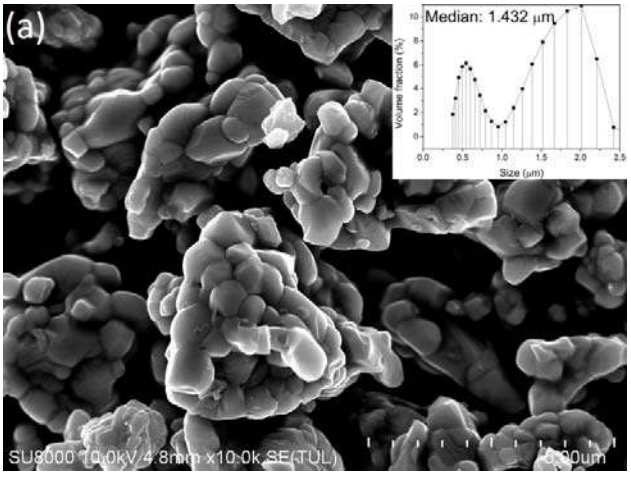

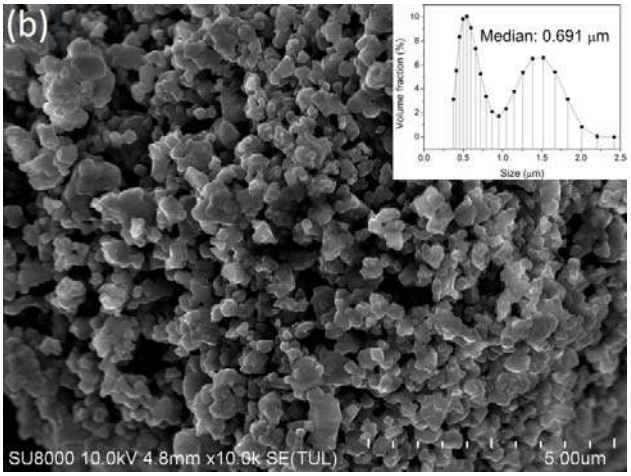

Figure 2. SEM micrographs of the as-prepared (a) LTO-1, and (b) LTO-2 powders. Particle size distributions are shown inset.

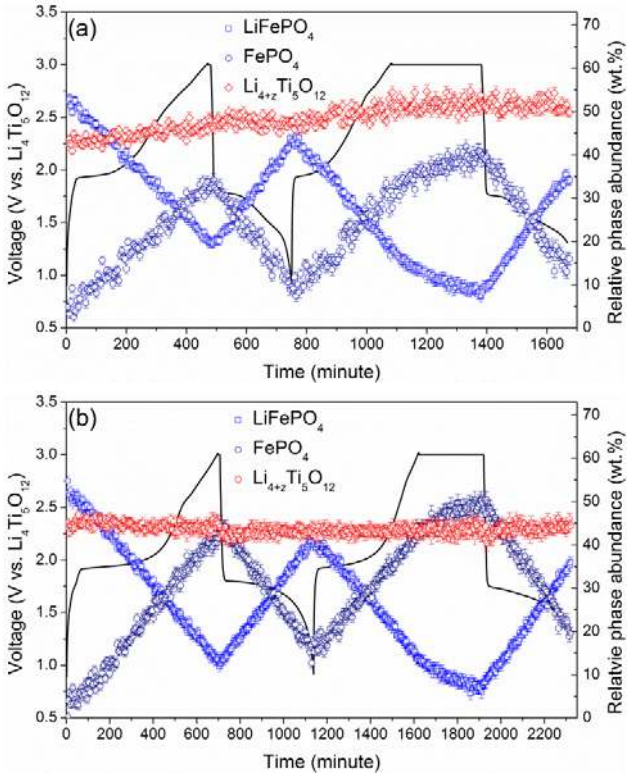

Figure 3. Relative phase abundance of the $LiFePO_4$ (blue), $Li_4Ti_5O_{12}$ (red), and delithiated $FePO_4$ (dark blue) phases upon cycling of battery-1 (a) and battery-2 (b). The total amount of active phase (cathode and anode) is normalized to 100%. Battery voltage is also shown.

During the first cycle of LTO-1, the lattice parameter increases to 8.3619(5) Å after 135 minutes of charge (a 0.03(1)% increase), followed by a decrease to 8.3584(6) Å at 420 minutes (a 0.04(1)% decrease), followed again by a sudden increase to 8.3600(6) Å (a 0.02(1)% increase) at the end of first charge (3.0 V vs. $Li_4Ti_5O_{12}$). On discharge, the lattice parameter drops to 8.3572(6) Å (a 0.03(1)% decrease) and then monotonically increases to 8.3613(6) Å (increasing by 0.05(1)%) at the end

of discharge. The sudden decrease in the lattice parameter at the beginning of delithiation is observed when the sign of the applied current changes. For LTO-2, the lattice parameter increases to 8.3649(5) Å after 110 minutes of charge (a 0.01(1)% increase), followed by a linear decrease to 8.3603(6) Å (a 0.05(1)% decrease) at 710 minutes (the end of charge at 3.0 V vs. $Li_4Ti_5O_{12}$). On discharge, the LTO-2 lattice parameter linearly increases to 8.366(5) Å (by 0.07(1)%) at 1140 minutes (1.0 V vs. $Li_4Ti_5O_{12}$), but we note that the sudden decrease in the lattice parameter observed for LTO-1 at the beginning of delithiation is not observed for LTO-2. The larger change in lattice parameter and the higher capacity achieved for LTO-2 compared with LTO-1 suggest that more Li^+ are accommodated in the LTO-2 anode, a result correlated to the smaller LTO-2 particle size. Given that the particle size is proportional to the length of the mean free Li^+ diffusion path,[13-17] this likely enables more Li^+ to migrate in LTO-2 than in LTO-1 in the same time-period.

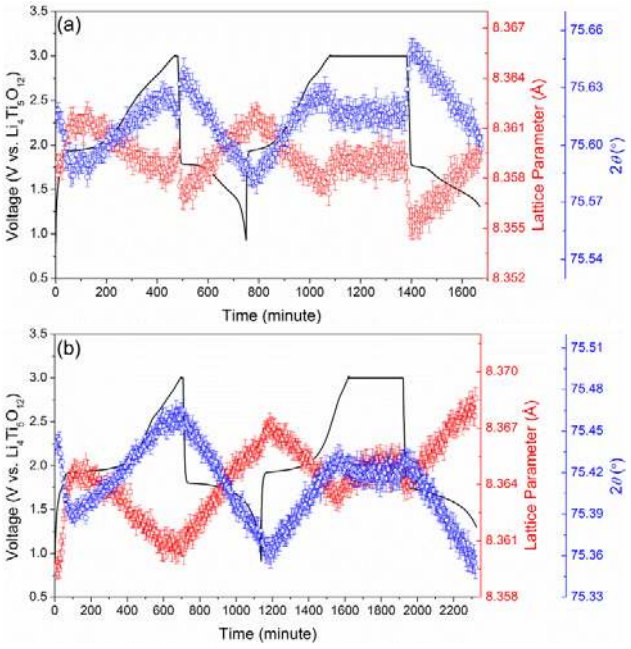

Figure 4. Variation of the LTO-1 (a) and LTO-2 (b) lattice parameter (red) and 222 reflection intensity (blue) during charge-discharge cycling. Battery voltage is also shown.

During the second cycle, similar variations in the LTO-1 and LTO-2 lattice are observed as the first cycle, with the exception of the 5 hour potentiostatic step. At the start of the potentiostatic step (3.0 V vs. $Li_4Ti_5O_{12}$), the current drops significantly and the gained capacity increases slowly (see **Figure S6**). Consequently, the lattice parameter of both anodes changes very little. At the end of the potentiostatic step both anodes exhibit a sudden increase in their lattice, although this feature is less pronounced for LTO-2. Given the higher capacity of LTO-2 it is possible that the LTO-1 lattice increase occurring during the first charge process takes place in LTO-2, but is occurring too quickly to be captured in the NPD data. We note that although the LTO-1 and LTO-2 lattice response during the same electrochemical charge and discharge are slightly different from each other, the LTO-1 and LTO-2 are structurally similar. According to Vegard's law,[36, 37] the slightly different LTO-1 and LTO-2 lattice parameter evolution likely reflect differences in Li content during battery cycling. A consideration of the lattice evolution in terms of the battery state-of-charge (SOC) for the first charge shows that although the LTO-2 lattice changes faster than that of LTO-1, the lattice parameter variation follow similar trends. Both $Li_{4+z}Ti_5O_{12}$ lattices undergo expansion up to 15% SOC, followed by a gradual contraction, and lastly followed again by expansion (last 5% SOC) (**Figure S7**). Quantitatively, we note that during the gradual contraction observed from approximately 15-90% SOC the LTO-2 lattice changes 28.8(7)% more quickly than that of LTO-1. We note again that the different variation of lattice parameters of LTO-1 and LTO-2 during charge/discharge reflects differences in Li distribution during lithiation and delithiation, and the lattice relaxation at the beginning of delithiation observed in LTO-1, but not in LTO-2, may arise as a result of this.

As a first approach to understanding the variation of Li in $Li_{4+z}Ti_5O_{12}$ during charge/discharge cycling we examined the changes in intensity of particular $Li_{4+z}Ti_5O_{12}$ reflections. **Figure 5** shows the intensity of the LTO-1 and LTO-2 222 and 004 reflections as a function of lithiation, where the 222 reflection intensity increases and the 004 reflection decreases, during lithiation.

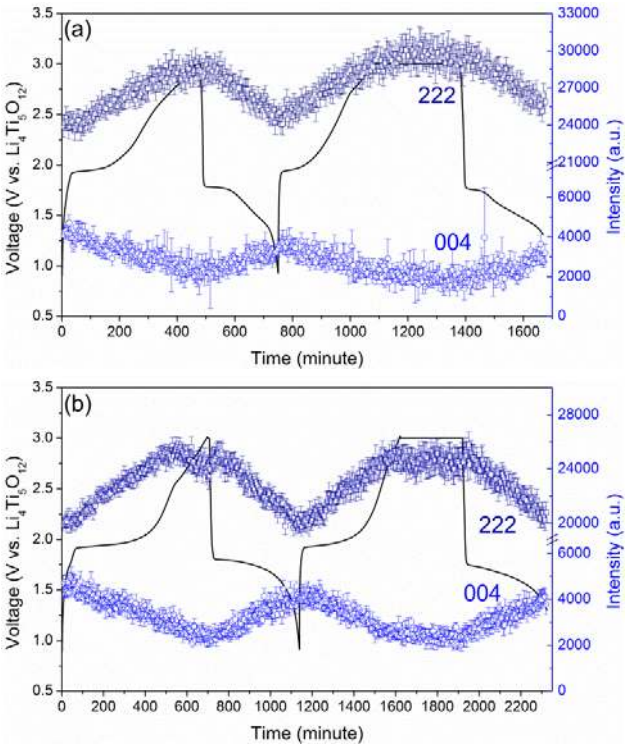

Figure 5. Variation of $Li_4Ti_5O_{12}$ 222 and 004 reflection intensities for LTO-1 (a) and LTO-2 (b), shown in **Table S1** during the first charge. Battery voltage is also shown.

Given that the $Li_4Ti_5O_{12}$ (222) plane is filled by Ti and Li atoms at the 16*d* site, both atoms having a negative coherent neutron-scattering length (-1.9 and -3.438 fm, respectively) and the $Li_4Ti_5O_{12}$ (004) plane is filled with O atoms at the 32*e* site having a positive coherent neutron-scattering length (5.803 fm) (**Figure 6**), the inserted and re-positioned Li needs

to occupy a site common to both planes to result in the observed intensity changes during lithiation, this being the 16*c* site. This observation is consistent with the reported $Li_4Ti_5O_{12}$-$Li_7Ti_5O_{12}$ transition mechanism where the inserted Li occupies the 16*c* site upon forming $Li_{4+z}Ti_5O_{12}$ ($Li_7Ti_5O_{12}$).[3, 4, 12, 17] Whilst the general trend of the $Li_4Ti_5O_{12}$ 004 and 222 reflection intensity change during lithiation is common between LTO-1 and LTO-2, there is a slight discrepancy between when the maximum intensity occurs, with the LTO-2 achieving the apparent saturation earlier, indicating that the Li site occupation differs between the anodes, most likely a phenomenon correlated to the greater capacity of battery-2.

Rietveld refinement of the $Li_{4+z}Ti_5O_{12}$ structure using the in-situ NPD data revealed Li occupation at the 8*a* and 16*c* sites (see **Figure 6**), consistent with that expected and also with the changes in reflection intensity discussed above. Extracting Li site occupancy factors in $Li_4Ti_5O_{12}$ from the in-situ NPD data is difficult, and to achieve this it was necessary to constrain the structure by fixing the O positional parameter (to 0.265 = *x* = *y* = *z*), although in reality the Li site occupation is known to influence the O position. We refine the O positional parameter using the in-situ NPD data in a separate analysis to reveal the average valence of the Ti, as discussed later. Nevertheless, the trends in Li site occupancy factors at the 8*a* and 16*c* sites extracted from the Rietveld refinement are consistent with that expected during the battery charge/discharge cycling (**Figure 7**).

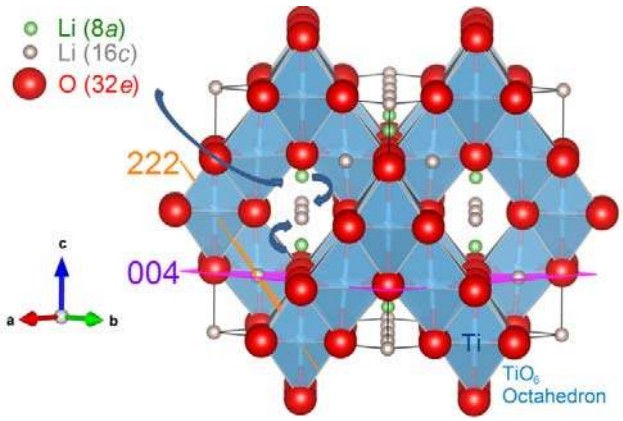

Figure 6. Crystal structure of $Li_{4+z}Ti_5O_{12}$ with the (222) and (004) planes indicated. The theoretical pathway of Li (inward) diffusion during lithiation is indicated by dark blue arrows. Ti is located at the center of the TiO_6 octahedra (16*d* site).

At the end of the lithiation process the site occupancy factors for Li at the 8*a* and 16*c* site are 0.46(26) and 1.20(23) in LTO-1, respectively, forming $Li^{8a}_{0.46(26)}Li^{16c}_{1.20(23)}(Li_{1/3}Ti_{5/3})^{16d}O^{32e}_4$. At the potentiostatic step (3.0 V vs. $Li_4Ti_5O_{12}$) during the second charge, the current drops significantly and the gained capacity increases slowly with a slower lithiation rate compared to that of the galvanostatic charge, in agreement with the observed lattice parameter variation. The Li content in each $Li_{4+z}Ti_5O_{12}$ should be proportional to the battery capacity. Given that the amount of LTO-1 in the cell is approximately about 680 mg and the charge capacity is 87.7 mA h (**Figure S6**), the final LTO-1 stoichiometry is expected to be $Li_{1.74}(Li_{1/3}Ti_{5/3})^{16d}O^{32e}_4$. The Rietveld-derived site occupancy factors for Li within calculation errors are in agreement with this expected value, although we note that the Rietveld-derived content accounts only for Li that is ordered within the $Li_{4+z}Ti_5O_{12}$ structure. In LTO-2 Li at the 16*c* site reaches a site occupancy factor of 1.47(30) at the end of lithiation, forming $Li^{8a}Li^{16c}_{1.47(43)}(Li_{1/3}Ti_{5/3})^{16d}O^{32e}_4$ ($Li_{7.41(\pm1.3)}Ti_5O_{12}$). Although the deviation from the calculated charge capacity is relatively large, the composition $Li_{7.25}Ti_5O_{12}$ is expected where the calculated and expected Li content are in agreement.

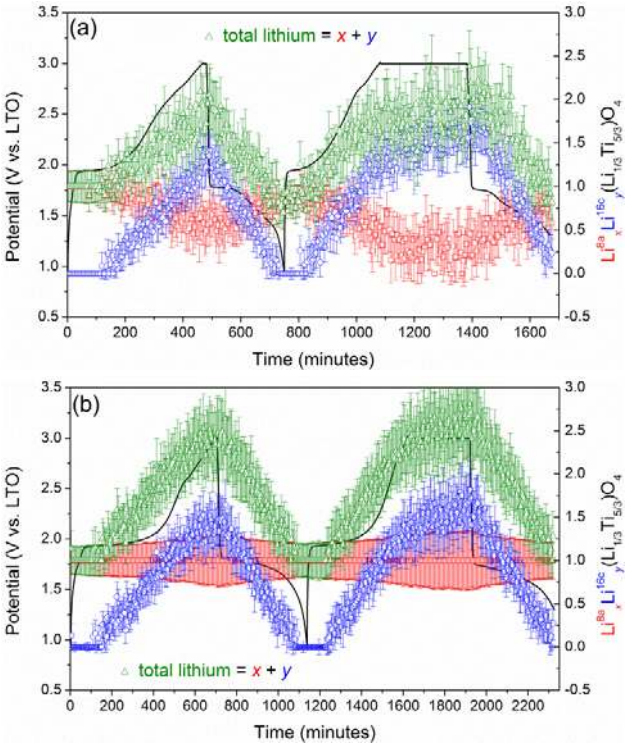

Figure 7. Li 8*a* and 16*c* site occupation and total Li content in LTO-1 (a) and LTO-2 (b) during charge-discharge cycling. Battery voltage is also shown.

Differences between the time evolution of the Li site occupancy factors in LTO-1 and LTO-2 are noted (**Figure 7**). The rate of lithiation (and delithiation) within $Li_{4+z}Ti_5O_{12}$ was determined by a linear fit to the time evolution of the Li content, including the site occupancy factors (**Figures S8 and S9**). Li intercalation and de-intercalation rates for the first cycle of battery-1 are summarized in **Table 1**.

During initial lithiation both $Li_{4+z}Ti_5O_{12}$ structures begin with Li fully occupied at the 8*a* site, which continues during lithiation until Li starts to populate at the 16*c* site in both $Li_{4+z}Ti_5O_{12}$ structures, at 110 minutes (1.95 V vs. $Li_4Ti_5O_{12}$) for LTO-1 and essentially at the same time, at 105 minutes (1.92 V vs. $Li_4Ti_5O_{12}$), for LTO-2. The 16*c* sites populate (and depopulate during delithiation) at different rates in the two anodes. We find that Li at the 16*c* site increases at the rate of 0.0036(1) $Li \cdot min^{-1}$ (0.216(6) Li^+ per $Li_{4+z}Ti_5O_{12}$ per hour) in LTO-1 and at 0.0028(1) $Li \cdot min^{-1}$ in LTO-2. The lower rate of Li population on charge (and also we find on depopulation during discharge) of the 16*c* site in LTO-2 than in LTO-1 is unexpected given the higher capacity of LTO-2. This result,

extracted from Rietveld analysis of the in-situ NPD data, mimics the trend of the $Li_4Ti_5O_{12}$ 222 and 004 reflection intensities for LTO-1 and LTO-2, with the rates shown in **Table S4,** indicating a slower rate of change of these in LTO-2 relative to LTO-1. In LTO-1 during delithiation Li occupation at the 8*a* site increases at the rate of 0.060(6) Li^+ per LTO-1 per hour (0.0010(1), **Figure S8a**), but that at the 16*c* site decreases at the faster rate of 0.297(1) Li^+ per LTO-1 per hour until the end of the battery discharge.

Population of the 16*c* site with Li in LTO-1 is accompanied by a depletion of Li at the 8*a* site at the rate of 0.072(6) Li^+ per $Li_{4+z}Ti_5O_{12}$ formula unit per hour (0.0012(1) $Li \cdot min^{-1}$), indicating that Li is migrating from 8*a* to 16*c* sites. Interestingly, in LTO-2 the Li site occupancy factor at the 8*a* site remains saturated (full occupation), although we note that the estimated standard deviation associated with the Li 8*a* site occupancy factor in LTO-2 increases as the lithiation proceeds (varying between 0.024 and 0.307). This result supports the theory that smaller particle sizes in $Li_{4+z}Ti_5O_{12}$ lead to larger capacities because the simultaneous 8*a* and 16*c* occupation is more easily accommodated in the near-surface region of the particle compared to the bulk.[18] There are two explanations for our observation of a static Li site occupancy factor at the 8*a* site in LTO-2, the first is that the 8*a* site is being refilled from the electrolyte at a higher rate than the rate of transfer of Li to the 16*c* site, and the second is that the 8*a* site does not participate in the electrochemical reaction. Our results indicate that the 8*a* site is being replenished during lithiation faster in LTO-2 than in LTO-1, based on the following arguments:

1. According to Vegard's law[36, 37] and our previous in-situ NPD analysis of electrodes,[21-25] the non-monotonic change in the $Li_{4+z}Ti_5O_{12}$ lattice reflects variation of Li occupation at the 8*a* and 16*c* sites in the $Li_{4+z}Ti_5O_{12}$. The similar variation of the LTO-1 and LTO-2 lattices as a function of state-of-charge (Figure S2) indicate that the Li sites are populated similarly and that the lithiation-delithiation processes are similar.
2. The smaller particle-size of LTO-2 results in a shorter mean free-path for Li^+ diffusion, which when combined with the slower rate of population of the 16*c* site in LTO-2 relative to LTO-1, results in the rate of transfer out of the 8*a* site being less than the rate of its repopulation.

Together with the observed increase in lattice parameter during initial lithiation (see **Figure 4**), the presence of Li at the 8*a* site and absence of Li at the 16*c* site in both anodes may suggest alternative pathways for the inward diffusion of Li^+, although the determination of such pathways is difficult using the in-situ NPD data. Laumann *et al*.[38] suggest that Li diffusion between the 8*a* and 16*c* sites occurs via the 32*e* site and Wilkening *et al*. suggest that a 48*f* site may be involved in the migration of Li within $Li_4Ti_5O_{12}$.[39] To consider these possibilities, we examine the Fourier-difference nuclear density maps using the refined $Li_{4+z}Ti_5O_{12}$ phases with the Li at 8*a* and 16*c* sites removed and NPD data taken at the charged, half-charged, and discharged states, summed over two datasets (a total of 10 minutes at each SOC), see **Figure 8**.

The Fourier-difference maps overlayed with the $Li_{4+z}Ti_5O_{12}$ structures with Li at 8*a* and 16*c* sites removed at the three SOC reveal no significant difference between the path for Li diffusion in LTO-1 and LTO-2. The results shown in Figure 9 do not support Li at the 48*f* site, with the view along the c-axis in **Figure S10** showing clearly an absence of residual nuclear density surrounding this site. However, a small amount of residual negative nuclear density surrounds the 32*e* site, indicating the possibility that this site is involved in the Li diffusion path, perhaps acting as a bridge connecting the 8*a* and 16*c* sites and lowering the energy barrier for diffusion as suggested by Laumann *et al*.[38] The depth of density in **Figure 8** represents the relative abundance of Li at each site, with the exception of the 16*d* site that is also occupied by Ti, where Ti also has a negative neutron-scattering length. The evolution of the density distribution on going from the charged to discharged states (during delithiation) reveals that for both anodes the Li concentration at 8*a* sites relatively increases, whereas the Li concentration at the 16*c* site decreases, showing good agreement with the calculated site occupation of Li at 8*a* and 16*c* (**Figure 7**). We note that the relative concentration of Li at the 8*a* and 16*c* sites differs significantly between LTO-1 and LTO-2, corroborating our result of dissimilarities in the lattice parameter evolution of LTO-1 and LTO-2. For example, at the half-charged state it can be seen that although both anodes have similar nuclear-density shapes, the site with most intense negative density differs for LTO-1 and LTO-2, where the strongest negative density is found at the 8*a* site in LTO-1 and at the 16*c* site for LTO-2. Overall the maps again agree well with the evolution of the Li 8*a* and 16*c* site occupation shown in **Figure 7**.

During battery charge, the anode is reduced and the Ti valence drops from 4^+ to 3.4^+ when forming $Li_7Ti_5O_{12}$ and to 3^+ when forming the Li-excess $Li_9Ti_5O_{12}$. The coulumbic attraction between Ti and O increases with Ti valence, as reflected by Ti-O bond length changes. Using the approach taken in our previous work,[21] we correlate the change in the O positional parameter to the Ti oxidation state and this to the $Li_4Ti_5O_{12}$ 222 and 004 reflection intensity.

To effectively track the O positional parameter it was necessary to fix the Li occupancy at 8*a* and 16*c* sites in the sequential Rietveld refinement. The variation of the O positional parameter in LTO-1 and LTO-2 during battery cycling is shown in **Figure 9**. It can be seen that the O atom moves further from the Ti atom as the average Ti valence decreases during charge and that this change is associated with changes in the measured $Li_{4+z}Ti_5O_{12}$ 222 and 004 reflection intensities. The O positional parameter and $Li_{4+z}Ti_5O_{12}$ 222 reflection intensity changes during charge/discharge help to complete the picture of the $Li_4Ti_5O_{12}$ structural changes in the $LiFePO_4||Li_4Ti_5O_{12}$ cell. By combining the evolution of $Li_{4+z}Ti_5O_{12}$ lattice and the O positional parameters with battery cycling we can calculate the Ti-O bond length. We estimate the valence of Ti at the 16*d* site during the battery charge and discharge using the bond-valence sum (BVS) method,[40] noting that the method will yield an approximate Ti valence as the Ti shares the 16*d* site with Li. The ideal Ti^{4+}-O^{2-} bond-length of 1.815 Å and empirical constant of 0.37 Å[40] are used in this estimation. The BVS of Ti in $Li_{4+z}Ti_5O_{12}$ during battery charge-discharge is shown in **Figure 10**, which reveals a decrease in Ti valence during lithiation (reduction during charge) and increase during delithiation (oxidation during discharge), as expected.

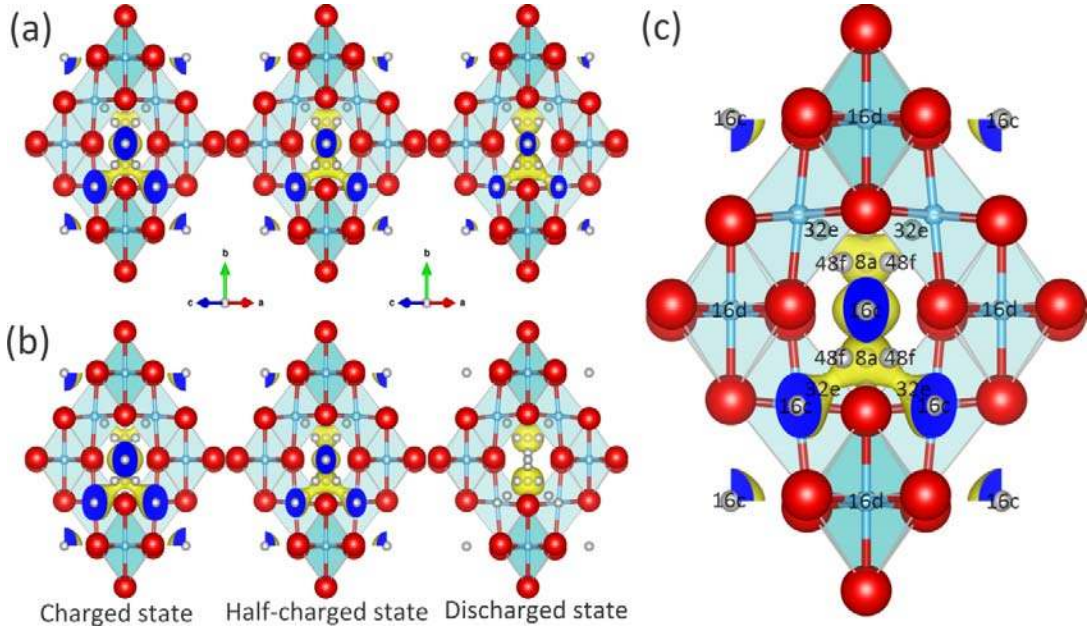

Figure 8. Fourier-difference maps showing only negative nuclear density (yellow) overlayed with the refined $Li_{4+z}Ti_5O_{12}$ structure for a) battery-1 and b) battery-2 at various battery SOC. For LTO-1, the NPD data were taken at 480-490, 605-615, and 740-750 minutes representing the charged, half-charged, and discharged states, respectively. For LTO-2, these states corresponded to data at 705-715, 895-905, and 1135-1145 minutes, respectively. The maps show half the view of the full unit cell shown in Figure 6 with the view along the c-axis shown in Figure S10. O atoms are shown in red, Li in grey with sites marked as for the LTO-1 half-charged figure, and Ti and Li at the 16*d* site are shown in cyan (and marked). The contour levels (yellow) are adjusted to be the same for direct comparison. A larger image detailing Li sites is also shown (c) using the result for LTO-1 at the half-charged state.

Table 1. Li intercalation and de-intercalation rates* in LTO-1 and LTO-2 during the first cycle.

	Li intercalation rate		Li de-intercalation rate		Total Li content ($x + y$)	
	$Li^+/Li_{4+z}Ti_5O_{12}$/min	$Li^+/Li_{4+z}Ti_5O_{12}$/h	$Li^+/Li_{4+z}Ti_5O_{12}$/min	$Li^+/Li_{4+z}Ti_5O_{12}$/h	Expected	Calculated
LTO-1	0.00234(2)	0.140(1)	0.00427(23)	0.256(14)	1.74	1.67(35)
LTO-2	0.00281(4)	0.169(2)	0.00450(3)	0.270(1)	2.09	2.47(43)

*Obtained from linear fits to the site occupancy factors or total $x + y$ in $Li^{8a}_{x}Li^{16c}_{y}(Li_{1/3}Ti_{5/3})^{16d}O^{32e}_{4}$ as a function of time (**Figure S8 and S9**).

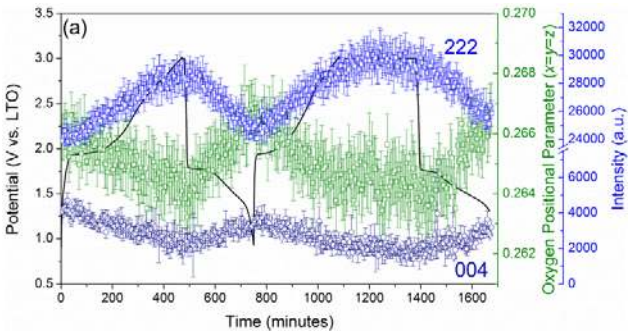

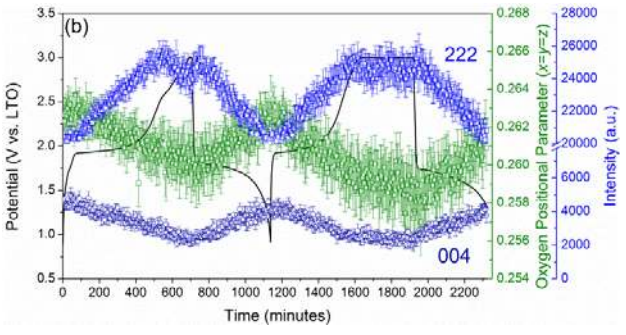

Figure 9. O positional parameter and $Li_{4+z}Ti_5O_{12}$ 222 and 004 reflection intensity in LTO-1 (a) and LTO-2 (b) during battery charge and discharge. Battery voltage is also shown.

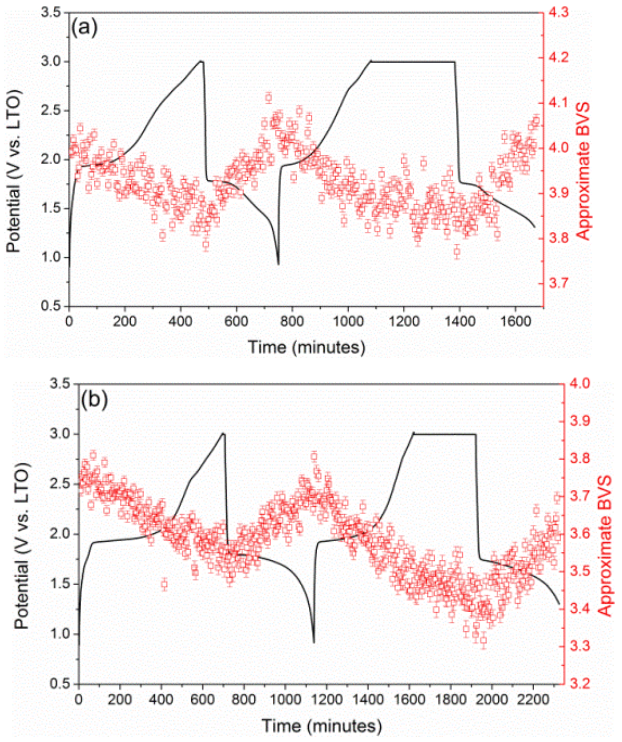

Figure 10. Approximate BVS for Ti in LTO-1 (a) and LTO-2 (b) during battery charge and discharge. Voltage is also shown.

■ CONCLUSIONS

Neutron-friendly $LiFePO_4$||$Li_4Ti_5O_{12}$ cells were used in an in-situ neutron powder diffraction study of two $Li_4Ti_5O_{12}$ anodes with differing particle sizes during charge-discharge battery cycling. By modelling the near zero-strain $Li_4Ti_5O_{12}$ material as a solid-solution reaction we reveal the underlying mechanism for particle-size induced changes in battery performance. The variation of lattice parameter, site-dependent Li concentration, and the oxidation state of Ti (the redox-active transition metal) in the anodes was monitored, and all point to an increase in the number of Li-ions migrating as a result of the reduced path length in the smaller particle-sized anode rather than a change in Li migration pathway. The lattice of both anodes during continuous lithiation undergoes expansion, followed by a gradual contraction, before expanding again. We reconcile the measured lattice parameter changes with our measurement of Li at specific sites within the $Li_4Ti_5O_{12}$ crystal structure, finding that Li migrates from the 8*a* to 16*c* sites in both anodes. Despite the similar trends of $Li_4Ti_5O_{12}$ lattice evolution and Li location during battery cycling, we note that the smaller particle-sized anode undergoes a much faster rate of change, 20.7(3)% during lithiation and 5.5(14)% during delithiation, than its larger particle-sized counterpart, consistent with the larger measured capacity.

Our analysis of Fourier-difference nuclear-density maps also indicate that the 32*e* site is involved in the Li diffusion in both anodes, but does not evidence participation of a 48*f* site in this.

Neutron powder diffraction is again shown to be an excellent tool for the study of electrode materials for Li-ion batteries, particularly when used to probe the real-time crystallographic changes of the materials in an operating battery during charge-discharge cycling.

ASSOCIATED CONTENT

Crystallographic details of the as-prepared samples (Table S1) and of the $Li_{4+z}Ti_5O_{12}$ used in the in-situ analysis (Table S2). Figures-of-merit for sequential refinements (Table S3). The rate of change of LTO 222 and 004 reflection intensity (Table S4). Figures include the Rietveld profile fit and SEM micrograph for the LiFePO4 (Figures S1 and S2, respectively. Sequential NPD patterns of battery-1 and battery- during cycling (Figure S3). In-situ NPD single-peak fitting results and electrochemical behavior of the $LiFePO_4$ cathode in battery-1 and battery-2 (Figure S4). Rietveld profiles for the as-prepared battery-1 and battery-2 samples (Figure S5). Charge-discharge curves and the calculated capacities for battery-1 and battery-2 during the NPD experiment (Figure S6). Linear fits of the lattice parameter of LTO-1 and LTO-2 as a function of state-of-charge (Figure S7), results from linear fits to the charge/discharge evolution of Li content in LTO-1 and LTO-2 (Figure S8 and S9, respectively), and the Fourier-difference nuclear density maps overlayed with the LTO-1 and LTO-2 structures shown along the c-axis (Figure S10). This material is available free of charge via the Internet at http://pubs.acs.org.

AUTHOR INFORMATION

Corresponding Author

* Email: vanessa.peterson@ansto.gov.au (V.K.P.) Tel: +61 9717 9401
* Email: shwu@ttu.edu.tw (S.-h.W.) Tel.: +886-2-25922458; Fax: +886-2-25936897,

Author Contributions

The manuscript was written through contributions of all authors. All authors have given approval to the final version of the manuscript.

ACKNOWLEDGMENT

The authors acknowledge the travel support funded by National Synchrotron Radiation Research Center (2013-3-100-1). The authors are also grateful to Professor Lin, Jeng-Yu of Tatung University for providing $Li_4Ti_5O_{12}$ sample, Tatung Fine Chemicals Co., Taiwan for providing $LiFePO_4$ sample and the staff members at the Bragg Institute, ANSTO for their operations support.

ABBREVIATIONS

NPD, neutron powder diffraction; LIB, Li-ion battery; BVS, bond-valence summation; LAMP, Large-array manipulation program; SOC, state-of-charge.

REFERENCES

1. Nishi, Y., *J. Power Sources* **2001,** 100, (1–2), 101-106.
2. Ohzuku, T.; Ueda, A.; Yamamoto, N., *J. Electrochem. Soc.* **1995,** 142, (5), 1431-1435.
3. Scharner, S.; Weppner, W.; Schmid-Beurmann, P., *J. Electrochem. Soc.* **1999,** 146, (3), 857-861.
4. Panero, S.; Reale, P.; Ronci, F.; Scrosati, B.; Perfetti, P.; Rossi Albertini, V., *Phys. Chem. Chem. Phys.* **2001,** 3, (5), 845-847.
5. Cho, J.; Kim, Y. J.; Kim, T.-J.; Park, B., *Angew. Chem.* **2001,** 113, (18), 3471-3473.
6. Ronci, F.; Reale, P.; Scrosati, B.; Panero, S.; Rossi Albertini, V.; Perfetti, P.; di Michiel, M.; Merino, J. M., *J. Phys. Chem. B* **2002,** 106, (12), 3082-3086.

7. Wang, C.; Appleby, A. J.; Little, F. E., *Electrochim. Acta* **2001,** 46, (12), 1793-1813.
8. Shu, J., *Electrochem. Solid-State Lett.* **2008,** 11, (12), A238-A240.
9. He, Y.-B.; Tang, Z.-Y.; Song, Q.-S.; Xie, H.; Liu, Y.-G.; Xu, Q., *J. Electrochem. Soc.* **2008,** 155, (7), A481-A487.
10. Shen, L.; Zhang, X.; Uchaker, E.; Yuan, C.; Cao, G., *Adv. Energy Mater.* **2012,** 2, (6), 691-698.
11. Bruce, P. G.; Scrosati, B.; Tarascon, J.-M., *Angew. Chem.* **2008,** 47, (16), 2930-2946.
12. Wagemaker, M.; Simon, D. R.; Kelder, E. M.; Schoonman, J.; Ringpfeil, C.; Haake, U.; Lützenkirchen-Hecht, D.; Frahm, R.; Mulder, F. M., *Adv. Mater.* **2006,** 18, (23), 3169-3173.
13. Striebel, K.; Shim, J.; Srinivasan, V.; Newman, J., *J. Electrochem. Soc.* **2005,** 152, (4), A664-A670.
14. Zhu, G.-N.; Wang, Y.-G.; Xia, Y.-Y., *Energy Environ. Sci.* **2012,** 5, (5), 6652-6667.
15. Jiang, C.; Hosono, E.; Ichihara, M.; Honma, I.; Zhou, H., *J. Electrochem. Soc.* **2008,** 155, (8), A553-A556.
16. Guo, X.; Wang, C.; Chen, M.; Wang, J.; Zheng, J., *J. Power Sources* **2012,** 214, (0), 107-112.
17. Cho, W.; Song, J. H.; Park, M.-S.; Kim, J.-H.; Kim, J.-S.; Kim, Y.-J., *J. Electrochem. Sci. Tech.* **2010,** 1, (2), 85-91.
18. Borghols, W. J. H.; Wagemaker, M.; Lafont, U.; Kelder, E. M.; Mulder, F. M., *J. Am. Chem. Soc.* **2009,** 131, (49), 17786-17792.
19. Cai, L.; An, K.; Feng, Z.; Liang, C.; Harris, S. J., *J. Power Sources* **2013,** 236, (0), 163-168.
20. Du, G.; Sharma, N.; Peterson, V. K.; Kimpton, J. A.; Jia, D.; Guo, Z., *Adv. Funct. Mater.* **2011,** 21, (20), 3990-3997.
21. Pang, W. K.; Sharma, N.; Peterson, V. K.; Shiu, J.-J.; Wu, S.-h., *J. Power Sources* **2014,** 246, (0), 464-472.
22. Sharma, N.; Du, G.; Studer, A. J.; Guo, Z.; Peterson, V. K., *Solid State Ionics* **2011,** 199–200, (0), 37-43.
23. Sharma, N.; Peterson, V. K., *Electrochim. Acta* **2013,** 101, (0), 79-85.
24. Sharma, N.; Reddy, M. V.; Du, G.; Adams, S.; Chowdari, B. V. R.; Guo, Z.; Peterson, V. K., *J. Phys. Chem. C* **2011,** 115, (43), 21473-21480.
25. Sharma, N.; Yu, D.; Zhu, Y.; Wu, Y.; Peterson, V. K., *Chem. Mater.* **2013,** 25, (5), 754-760.
26. Colin, J.-F.; Godbole, V.; Novák, P., *Electrochem. Comm.* **2010,** 12, (6), 804-807.
27. Padhi, A. K.; Nanjundaswamy, K. S.; Goodenough, J. B., *J. Electrochem. Soc.* **1997,** 144, (4), 1188-1194.
28. Padhi, A. K.; Nanjundaswamy, K. S.; Masquelier, C.; Okada, S.; Goodenough, J. B., *J. Electrochem. Soc.* **1997,** 144, (5), 1609-1613.
29. Liss, K.-D.; Hunter, B.; Hagen, M.; Noakes, T.; Kennedy, S., *Physica B* **2006,** 385–386, Part 2, (0), 1010-1012.
30. Hunter, B. *Rietica - A Visual Rietveld Program*, International Union of Crystallography Commission on Powder Diffraction Newsletter No. 20, (Summer) http://www.rietica.org: 1998.
31. Studer, A. J.; Hagen, M. E.; Noakes, T. J., *Physica B* **2006,** 385–386, Part 2, (0), 1013-1015.
32. Rodríguez-Carvajal, J., *Physica B* **1993,** 192, (1–2), 55-69.
33. T. Roisnel; Rodriguez-Carvajal, J. In *WinPLOTR: A Windows Tool for Powder Diffraction Patterns Analysis*, Materials Science Forum, Proceedings of the Seventh European Powder Diffraction Conference (EPDIC 7), 2000; R. Delhez; Mittenmeijer, E. J., Eds. 2000; pp 118-123.
34. Richard, D.; Ferrand, M.; Kearley, G. J., *J. Neutron Res.* **1996,** 4, (1-4), 33-39.
35. Palomares, V.; Goni, A.; Iturrondobeitia, A.; Lezama, L.; de Meatza, I.; Bengoechea, M.; Rojo, T., *J. Mater. Chem.* **2012,** 22, (11), 4735-4743.
36. Denton, A. R.; Ashcroft, N. W., *Phys. Rev. A* **1991,** 43, (6), 3161-3164.
37. Vegard, L., *Zeitschrift für Physik* **1921,** 5, (1), 17-26.
38. Laumann, A.; Boysen, H.; Bremholm, M.; Fehr, K. T.; Hoelzel, M.; Holzapfel, M., *Chem. Mater.* **2011,** 23, (11), 2753-2759.
39. Wilkening, M.; Amade, R.; Iwaniak, W.; Heitjans, P., *Phys. Chem. Chem. Phys.* **2007,** 9, (10), 1239-1246.
40. Brown, I. D.; Altermatt, D., *Acta Crystallogr. Sect. B* **1985,** 41, (4), 244-247.

Table of Contents